



MgATP hydrolysis destabilizes the interaction between subunit H and yeast V_1 -ATPase, highlighting H's role in V-ATPase regulation by reversible disassembly

Received for publication, March 16, 2018, and in revised form, April 22, 2018. Published, Papers in Press, May 12, 2018, DOI 10.1074/jbc.RA118.002951

Stuti Sharma, Rebecca A. Oot, and Stephan Wilkens¹

From the Department of Biochemistry and Molecular Biology, State University of New York (SUNY) Upstate Medical University, Syracuse, New York 13210

Edited by Karen G. Fleming

Vacuolar H^+ -ATPases (V-ATPases; V_1V_o -ATPases) are rotary-motor proton pumps that acidify intracellular compartments and, in some tissues, the extracellular space. V-ATPase is regulated by reversible disassembly into autoinhibited V_1 -ATPase and V_o proton channel sectors. An important player in V-ATPase regulation is subunit H, which binds at the interface of V_1 and V_o . H is required for MgATPase activity in holo-V-ATPase but also for stabilizing the MgADP-inhibited state in membrane-detached V_1 . However, how H fulfills these two functions is poorly understood. To characterize the H- V_1 interaction and its role in reversible disassembly, we determined binding affinities of full-length H and its N-terminal domain (H_{NT}) for an isolated heterodimer of subunits E and G (EG), the N-terminal domain of subunit *a* (a_{NT}), and V_1 lacking subunit H ($V_1\Delta H$). Using isothermal titration calorimetry (ITC) and biolayer interferometry (BLI), we show that H_{NT} binds EG with moderate affinity, that full-length H binds a_{NT} weakly, and that both H and H_{NT} bind $V_1\Delta H$ with high affinity. We also found that only one molecule of H_{NT} binds $V_1\Delta H$ with high affinity, suggesting conformational asymmetry of the three EG heterodimers in $V_1\Delta H$. Moreover, MgATP hydrolysis-driven conformational changes in V_1 destabilized the interaction of H or H_{NT} with $V_1\Delta H$, suggesting an interplay between MgADP inhibition and subunit H. Our observation that H binding is affected by MgATP hydrolysis in V_1 points to H's role in the mechanism of reversible disassembly.

Vacuolar H^+ -ATPases (V-ATPases²; V_1V_o -ATPases) are ATP-dependent proton pumps present in all eukaryotic cells.

This work was supported by National Institutes of Health Grant GM058600 and a Bridge Grant from SUNY Upstate Medical University (to S. W.). The authors declare that they have no conflicts of interest with the contents of this article. The content is solely the responsibility of the authors and does not necessarily represent the official views of the National Institutes of Health.

This article contains Figs. S1–S4.

¹ To whom correspondence should be addressed. Tel.: 215-464-8703; Fax: 315-464-8750; E-mail: wilkensk@upstate.edu.

² The abbreviations used are: V-ATPase, vacuolar H^+ -ATPase; V_1 , ATPase sector of the vacuolar ATPase; V_o , membrane sector of the vacuolar ATPase; a_{NT} , N-terminal cytoplasmic domain of the *a* subunit; BME, β -mercaptoethanol; MBP, maltose-binding protein; ITC, isothermal titration calorimetry; BLI, biolayer interferometry; TCEP, tris(2-carboxyethyl)phosphine; AMC, anti-mouse Fc capture; AMPPNP, 5'-adenylyl- β , γ -imidodiphosphate; NEM, N-ethylmaleimide; CB, column buffer; bis-Tris, 2-[bis(2-hydroxyethyl)amino]-2-(hydroxymethyl)propane-1,3-diol.

This is an open access article under the CC BY license.

10718 J. Biol. Chem. (2018) 293(27) 10718–10730

Typically, the V-ATPase is localized on the endomembrane system where the enzyme acidifies intracellular compartments, a process essential for pH homeostasis, protein trafficking, endocytosis, hormone secretion, mTOR signaling, and lysosomal degradation (1). The V-ATPase is also present on the plasma membrane of certain specialized cells such as osteoclasts, renal cells, the vas deferens, and the epididymis where the enzyme acidifies the extracellular environment. V-ATPase's proton pumping activity has been linked to numerous human diseases including osteoporosis and -petrosis (2, 3), renal tubular acidosis (4), male infertility (5), neurodegeneration (6), diabetes (7), viral infection (8), and cancer (9), making the enzyme a valuable drug target (10, 11).

The V-ATPase shares a similar architecture and catalytic mechanism with the F-ATP synthase such that it consists of a water-soluble ATP-hydrolyzing machine (V_1) and a membrane-integral proton channel (V_o), which are structurally and functionally coupled via a central stalk and multiple peripheral stalks (12–14). The subunit composition of the V-ATPase from yeast is $A_3B_3CDE_3FG_3H$ for the cytosolic V_1 (15) and $ac_8c'c''def$ for the membrane-integral V_o (16, 17). The subunit architecture of the V-ATPase has been studied by electron microscopy (EM) and several low- to intermediate-resolution reconstructions of bovine, yeast, and insect V-ATPase are available, which, together with X-ray crystal structures of individual subunits and subcomplexes of yeast V-ATPase and bacterial homologs, have provided a detailed model of the subunit architecture of the eukaryotic V-ATPase complex (17–22) (see Fig. 1A). V-ATPase is a rotary-motor enzyme (14). ATP hydrolysis in the catalytic A_3B_3 hexamer is coupled to rotation of the proteolipid ring ($c_8c'c''$) via a central rotor made of subunits D, F, and *d* with concurrent proton translocation at the interface of the proteolipid ring and the C-terminal domain of subunit *a* (a_{CT}). During rotary catalysis, the motor is stabilized by a peripheral stator complex consisting of three peripheral stalks constituted by heterodimers of subunits E and G (hereafter referred to as EG1–3) that connect the A_3B_3 hexamer to the N-terminal domain of the membrane-bound *a* subunit (a_{NT}) via the single-copy “collar” subunits H and C (19, 21) (see Fig. 1A). Three intermediates (referred to as rotational states 1–3), in which the central rotor is spaced 120° relative to the catalytic hexamer and subunit *a*, have been visualized in the yeast enzyme by cryo-EM (21).

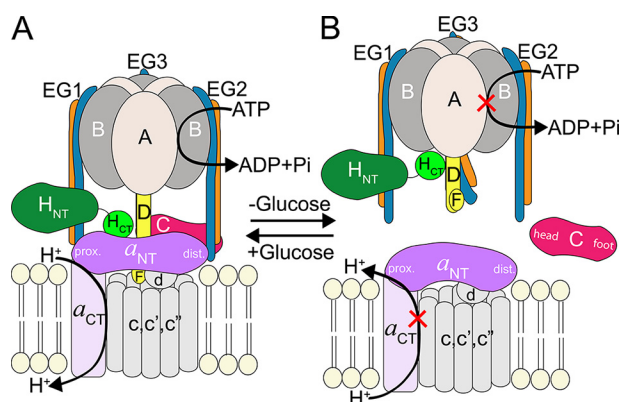


Figure 1. Schematic of yeast V-ATPase regulation by reversible disassembly. *A*, subunit architecture of holo-V-ATPase. The V_1 and V_o sectors are assembled and form an active enzyme. *B*, upon glucose deprivation, the V_1 and V_o sectors disengage, and the activity of both sectors is silenced. The subunits of the peripheral stator that form the V_1 - V_o interface are shown in color. *prox.*, proximal; *dist.*, distal.

Unlike the related F-ATP synthase, eukaryotic V-ATPase is regulated by a unique mechanism referred to as reversible disassembly wherein, upon receiving cellular signals, V_1 dissociates from V_o , and the activity of both sectors is silenced (22–26) (see Fig. 1*B*). Reversible disassembly was first observed in yeast (27) and insects (28), but the process has recently also been observed in higher animals including human (29–32). Studies in yeast have shown that, during enzyme disassembly, subunit C is released into the cytosol by an unknown mechanism and reincorporated during reassembly (27). Because of regulation of the V-ATPase by reversible disassembly, the peripheral stator subunit interactions at the V_1 - V_o interface draw particular attention as they must be sufficiently strong to withstand the torque generated during ATP hydrolysis, but at the same time they must be vulnerable enough to allow breaking on a timescale for reversible disassembly to occur efficiently.

We previously characterized the interaction of the collar subunit C with EG and a_{NT} and found that although the head domain of C (C_{head}) binds EG with high affinity (C_{head} -EG3; see Fig. 1*A*), its foot domain (C_{foot}) and EG both interact weakly with a_{NT} , resulting in a high-avidity ternary interface (EG2- a_{NT} - C_{foot}) in holo-V-ATPase (33, 34). Another collar subunit at the V_1 - V_o interface is subunit H, and although deletion of C prevents stable assembly of V_1 and V_o (35), deletion of H results in the formation of a V_1V_o (Δ H) complex that lacks MgATPase and proton-pumping activities (36, 37). Moreover, although C is released into the cytosol upon disassembly of V_1V_o , H remains stably associated with V_1 (Fig. 1*B*). The crystal structure of H revealed that it consists of a larger N-terminal (H_{NT}) and smaller C-terminal domain (H_{CT}) connected by a short linker (38). Previous functional characterization of H_{NT} and H_{CT} suggested that, although H_{NT} is required for MgATPase activity in V_1V_o , H_{CT} has a dual function in that it is required for both coupling of V_1 's ATPase activity to proton pumping in V_1V_o (37) and inhibition of MgATPase activity in membrane-detached V_1 (39). The dual role and functional separation of H_{NT} and H_{CT} along with differences in regulatory function compared with C are not well understood and prompted the analyses of the interactions of H, H_{NT} , and H_{CT} with its binding

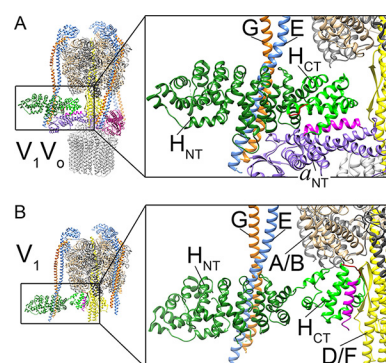


Figure 2. Binding interactions of subunit H in holo- V_1V_o and autoinhibited V_1 -ATPase. *A*, in V_1V_o (Protein Data Bank code 3J9U) (21), H_{NT} (dark green) is bound to EG1 (blue/orange), and H_{CT} (light green) is in contact with a_{NT} (purple). *B*, in membrane-detached and autoinhibited V_1 (Protein Data Bank code 5D80) (22), the contact between H_{NT} and EG1 is preserved, but H_{CT} undergoes a ~150° rotation to bind the bottom of the A_3B_3 hexamer and the rotor subunit D. The large conformational change in H_{CT} is depicted by the positions of the C-terminal α -helix (magenta) and the inhibitory loop (red) in holo- V_1V_o versus autoinhibited V_1 -ATPase.

partners in V_1 and V_o . We therefore used recombinant H, H_{NT} , and H_{CT} for quantification of their interactions with purified EG, a_{NT} , and V_1 lacking subunit H ($V_1\Delta$ H) using isothermal titration calorimetry (ITC) and bilayer interferometry (BLI). We found that H_{NT} binds no more than one of the three EGs on $V_1\Delta$ H and that the affinity of this interaction is ~40-fold higher than that between H_{NT} and isolated EG, suggesting that H_{NT} prefers a particular conformation of EG on V_1 . We further found that full-length H interacts with $V_1\Delta$ H with an ~70-fold higher affinity than H_{NT} , indicative of a significant contribution of H_{CT} to the binding energy. Furthermore, we show that MgATP hydrolysis-driven conformational changes in the catalytic A/B pairs, the central rotor (DF), and the peripheral stalks (EG) destabilize the V_1 -H interaction until inhibitory MgADP is trapped in a catalytic site. The findings are discussed in context of the mechanism of V-ATPase regulation by reversible disassembly.

Results

Expression, purification, and biophysical characterization of H, H_{NT} , H_{CT} , and $a_{NT}(1-372)$

To understand the role of the V_1 - V_o interface in the mechanism of reversible disassembly, our laboratory has previously characterized the interactions among C_{head} , C_{foot} , EG, and a_{NT} (33, 34). Interactions involving subunit H, however, are yet to be quantified. Pulldown and yeast two-hybrid assays have shown that H is able to bind the N-terminal region of subunit E (40). In addition, EM and crystal structures of V_1V_o and V_1 , respectively, show H_{NT} bound to one of the three EG peripheral stalks (EG1; see Fig. 2, *A* and *B*), whereas H_{CT} is seen to either rest on the coiled-coil middle domain of a_{NT} (in V_1V_o ; Fig. 2*A*) or at the bottom of the A_3B_3 hexamer (in autoinhibited V_1) (Fig. 2*B*) (21, 22). To analyze the interactions of H within the enzyme in more detail, we expressed H, H_{NT} , and H_{CT} separately and quantified their interactions with recombinant EG, a_{NT} , and $V_1\Delta$ H purified from yeast.

Full-length H, H_{NT} (residues 1–354), H_{CT} (residues 352–478), and a_{NT} (residues 1–372) were expressed in *Escherichia*

Subunit H interactions at the V_1 - V_o interface

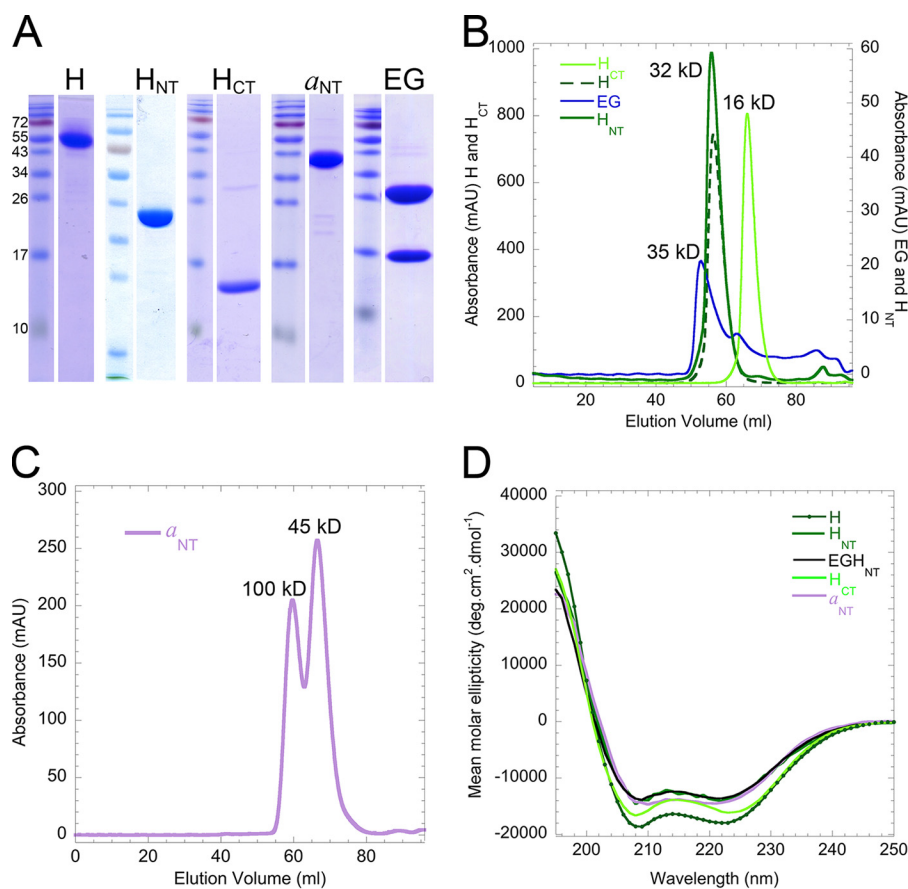


Figure 3. Purification and characterization of recombinant V-ATPase subunits and their domains. *A*, SDS-polyacrylamide gel of purified recombinant proteins used in the interaction studies described here. *B*, gel filtration elution profiles of H, H_{NT}, H_{CT}, and EG on a 1.6 × 50-cm Superdex 75 column. H, H_{NT}, and H_{CT} elute in single symmetric peaks (with molecular weights indicated next to the peaks), suggesting monomeric and monodisperse proteins. The majority of EG elutes as a single peak with some residual excess G subunit at larger elution volumes. *C*, a_{NT}(1–372) elutes on a 1.6 × 50-cm Superdex 200 column in two overlapping peaks corresponding to the dimer and monomer as described before. *D*, CD spectra of H, H_{NT}, H_{CT}, a_{NT}, and the EGH_{NT} complex recorded from 250 to 195 nm. The minima at 222 and 208 nm indicate α -helical secondary structure. *deg*, degrees; *mAU*, milliabsorbance units.

coli as N-terminal fusions with maltose-binding protein (MBP). After amylose affinity capture, fusions were cleaved, and MBP was removed by ion exchange and size exclusion chromatography, resulting in purified subunits and subunit domains (Fig. 3A). All proteins eluted near their expected molecular masses on size exclusion chromatography except a_{NT}(1–372), which exists in a dimer–monomer equilibrium as described previously (26, 34) (Fig. 3, B and C). Consistent with available structural information, circular dichroism (CD) spectroscopy revealed a high degree of α -helical secondary structure, suggesting proper folding of the recombinant polypeptides (Fig. 3D).

Interaction of H_{NT} with EG

We previously established that binding of C (or C_{head}) to isolated EG occurs with high affinity and that the interaction greatly stabilizes EG (33). To further characterize the interactions at the V_1 - V_o interface, we set out to determine the affinity of the H_{NT}-EG interaction using ITC. Titration of H_{NT} into EG was exothermic, and the binding curve was fit to a single-binding-site model, revealing a K_d of the interaction of 187 nM. The binding enthalpy (ΔH) and entropy (ΔS) were -8 kcal/mol and 2.5 cal/(mol·K), respectively, with a concomitant free energy change (ΔG) of ~ -36 kJ/mol (Fig. 4A). Consistent with the ITC

titration, size exclusion chromatography of a mixture of EG and an excess of H_{NT} resulted in the formation of a ternary H_{NT}-EG complex (Fig. 4, B and C), and taken together, the data show that H_{NT} forms a stable complex with the EG heterodimer. Previously, we found that the EG's N-terminal right-handed coiled coil is thermally labile with a T_m of ~ 25 °C (Fig. 4D, blue trace) (29) and that the T_m of EG is increased by about 10 °C upon complex formation with C_(head) (33). To test whether H_{NT} binding has a similar stabilizing effect on EG, thermal unfolding of the individual proteins and EGH_{NT} complex was monitored by recording the CD signal at 222 nm as a function of temperature. The data show that isolated H_{NT} unfolds with an apparent T_m of ~ 63 °C (Fig. 4D, green trace). The thermal unfolding curve of the EGH_{NT} complex showed two transitions, one at 25 °C and one at 64 °C, suggesting that the stability of EG is not increased upon H_{NT} binding (Fig. 4D, black trace). Moreover, as also shown previously (33), isolated EG heterodimer dissociates during native agarose gel electrophoresis, whereas in presence of C_{head} the three proteins migrate as a heterotrimeric complex in the electric field. However, consistent with the thermal unfolding data, a complex of EGH_{NT} did not comigrate on the native gel but ran as three separate species (Fig. 4E). Therefore, although both C_{head} and H_{NT} form a

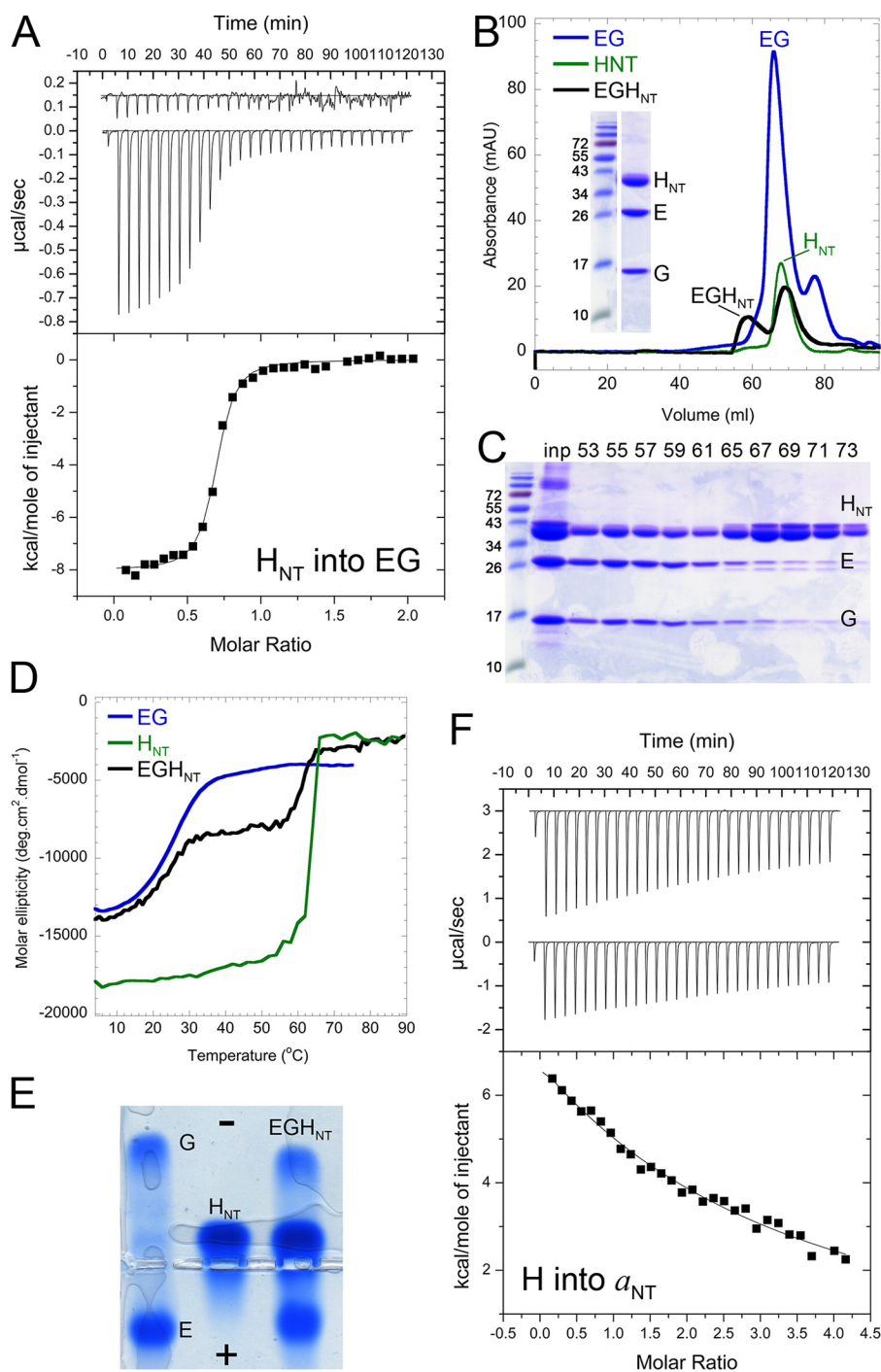


Figure 4. Interaction of H_{NT} with the EG heterodimer and H with a_{NT} . A, isothermal titration calorimetry of the interaction between H_{NT} and EG. H_{NT} was titrated into EG (top panel, lower trace) or buffer only (top panel, top trace), and the heat associated with the interaction was measured at 10°C in 20 mM Tris-HCl, 0.5 mM EDTA, 1 mM TCEP, pH 8. The area under the peaks in the top panel was integrated and plotted as kcal/mol of H_{NT} as a function of binding stoichiometry in the bottom panel. These data were fit using a one-site binding model resulting in a K_d of 187 nM with ΔH and ΔS values of -8 kcal/mol and 2.5 cal/(mol·K), respectively, resulting in a ΔG of the interaction of ~ -36 kJ/mol. A representative of three separate titrations is shown. B, the ITC cell content was subjected to gel filtration on a 1.6×50 -cm Superdex 200 column (black trace). The individual gel filtration elution profiles of H_{NT} and EG using the same column are shown in green and blue, respectively. C, SDS-PAGE of gel filtration fractions from the ITC cell content. EGH_{NT} elutes at higher molecular mass with excess H_{NT} in a well separated peak. The shift of the EGH_{NT} peak (compared with EG or H_{NT}) toward higher molecular weight indicates complex formation. The inset in B shows the EGH_{NT} peak fraction (fraction 55) from the SDS-PAGE gel of the ITC cell content shown in C. D, thermal unfolding of H_{NT} , EG, and EGH_{NT} monitored by recording the CD signal at 222 nm with increasing temperature. H_{NT} shows highly cooperative unfolding with an apparent T_m of $\sim 63^{\circ}\text{C}$ (green). EG has an apparent T_m of $\sim 25^{\circ}\text{C}$ (data taken from Ref. 33). The EGH_{NT} complex shows two unfolding transition with T_m values similar to the those observed for the individual proteins, suggesting that H_{NT} binding to EG does not stabilize the EG heterodimer. E, native agarose gel electrophoresis of EG heterodimer, H_{NT} , and EGH_{NT} . 30 μg of purified EG, 30 μg of purified H_{NT} , and a mixture of equimolar amounts of H_{NT} and EG (total 60 μg) were loaded. Unlike binding of C_{head} to EG (33), binding of H_{NT} does not appear to stabilize EG under these conditions. F, isothermal titration calorimetry of the interaction between a_{NT} and H. H was titrated into a_{NT} (top panel, lower trace) or buffer (top panel, top trace), and the heat associated with the interaction was measured at 10°C in 20 mM Tris-HCl, 0.5 mM EDTA, 1 mM TCEP, pH 8. Subtracting the heat of dilution of H into buffer revealed an endothermic binding reaction. Fitting the data (bottom panel) to a one-site binding model with a fixed $n = 1$ allowed an estimate of the K_d of ~ 130 μM . A representative titration from two repeats is shown. mAU, milliabsorbance units.

Subunit H interactions at the V_1 - V_o interface

stable complex with EG, the nature of the two interactions are strikingly different.

Interaction of H with a_{NT}

Prior work from our laboratory has shown that the EG2- a_{NT} - C_{foot} junction at the V_1 - V_o interface (Fig. 1A) is formed by multiple low-affinity interactions, and we reasoned that the sum of these interactions provides a high-avidity binding site between V_1 and V_o that could be targeted for regulated disassembly (34). Another interaction that is seen in EM reconstructions of the intact V-ATPase, and that must be broken and reformed during reversible disassembly, is between H and a_{NT} (Figs. 1A and 2A). To estimate the affinity between H and a_{NT} , we performed ITC experiments by titrating H into a_{NT} (1-372) (Fig. 4F). Subtracting the heat generated from diluting H into buffer from the heat generated from titrating H into a_{NT} (1-372) revealed a weak endothermic binding reaction between the two proteins. Fitting the data to a one-site binding model revealed a K_d of 135 μ M and ΔH , ΔS , and ΔG values of 4 kcal/mol, 36.1 cal/(mol·K), and -26 kJ/mol, respectively. Consistent with our ITC data, a mixture of H and a_{NT} eluted at the same volumes as the individual proteins on size exclusion chromatography (Fig. S1). The low-affinity interaction between H and a_{NT} supports our existing model that V_1 binds V_o via several low-affinity interactions that, taken together, result in a high-avidity interface in assembled V_1V_o .

Interaction of $V_1\Delta H$ with H, H_{NT} , and H_{CT} characterized by BLI

Previous experiments showed that H remains bound to V_1 even at the low concentrations used in enzyme assays (e.g. ~15 nM) (22, 25, 39) and under the conditions of electrospray ionization used for native MS (15). Although the data so far have shown that the affinity of H_{NT} for EG as measured using ITC is moderately high, the observed K_d of ~0.2 μ M (Fig. 4A) could not explain the above observations, which means that the interaction of H with V_1 has to be much stronger (39). We therefore wished to determine the affinity of full-length H as well as H_{NT} and H_{CT} for $V_1\Delta H$. The interaction between $V_1\Delta H$ and MBP-tagged H, H_{NT} , and H_{CT} was quantified using BLI. MBP-tagged proteins were immobilized on anti-mouse Fc capture (AMC) biosensors using an anti-MBP antibody, and the rate of association and dissociation of $V_1\Delta H$ was measured hereafter. The slow dissociation of MBP-tagged H, H_{NT} , and H_{CT} from the anti-MBP antibodies was subtracted from the $V_1\Delta H$ dissociation rates for analysis of the kinetic data. BLI experiments for measuring association and dissociation kinetics between $V_1\Delta H$ and MBP-H/ H_{NT} were conducted at five different $V_1\Delta H$ concentrations, and the resulting association and dissociation curves were fit to a global single-site binding model (Fig. 5, A and B). Analysis of the data for MBP-H and MBP- H_{NT} revealed K_d values of ~65 pM (Fig. 5A) and ~4.5 nM (Fig. 5B), respectively. We also tested the binding of $V_1\Delta H$ to MBP- H_{CT} , but we were not able to determine a K_d as there was no measurable association at low $V_1\Delta H$ concentrations (<100 nM), and higher $V_1\Delta H$ concentrations (e.g. 1 μ M) resulted in nonspecific binding to the BLI sensors (data not shown). Overall, the interaction of H_{NT} with EG as part of $V_1\Delta H$ was ~40-fold tighter when compared with the interaction between H_{NT} and isolated EG

(as measured using ITC; Fig. 4A), suggesting that the conformation of EG on $V_1\Delta H$ is more favorable for H_{NT} binding than the conformation(s) of isolated EG. In addition, although we could not detect an interaction between H_{CT} and $V_1\Delta H$ under the conditions of BLI, a ~70-fold higher affinity of $V_1\Delta H$ for H as compared with H_{NT} suggests a significant contribution of H_{CT} to the V_1 -H interaction. From our ITC and BLI experiments, we infer that the binding interaction between H_{NT} and EG allows H_{CT} to switch conformations so that it can either bind a_{NT} (in V_1V_o) or subunits B and D (in V_1) to efficiently carry out its dual role in reversible disassembly.

$V_1\Delta H$ binds no more than one H_{NT}

Because $V_1\Delta H$ contains three EG heterodimers, we wished to determine whether all three or only one of the EGs can bind H_{NT} . Purified $V_1\Delta H$ was mixed with a 5-fold molar excess of H_{NT} followed by size exclusion chromatography. Under these conditions, some H_{NT} coeluted with $V_1\Delta H$ with the excess H_{NT} eluting from the column as a separate, lower molecular weight peak (Fig. 5, C and D). The $V_1(\Delta H)H_{NT}$ complex was concentrated, and approximately equal amounts of $V_1\Delta H$ and $V_1(\Delta H)H_{NT}$ were resolved using SDS-PAGE. The staining of H_{NT} in the purified $V_1(\Delta H)H_{NT}$ complex was similar to that of single-copy subunits in the V_1 complex (for example subunit D), indicating that no more than one copy of H_{NT} bound to $V_1\Delta H$ (Fig. 5E). Therefore, although there are three EGs in $V_1\Delta H$, only one of these is in a conformation that is able to bind H_{NT} with high affinity, highlighting the conformational asymmetry of the peripheral stalks.

The interaction of H with $V_1\Delta H$ is destabilized upon MgATP hydrolysis

The preference of H_{NT} for one of three EGs suggested that the asymmetry of the peripheral stalks originates in the catalytic core (A_3B_3DF) of V_1 . Upon MgATP hydrolysis, however, the conformational changes of the catalytic sites from open to loose to tight drive counterclockwise rotation of the central rotor along with cyclic structural changes in the peripheral stalks from EG1 to EG3 to EG2 (41). In addition, based on the structure and nucleotide occupancy of the autoinhibited V_1 sector, our laboratory suggested that H_{CT} inhibits V_1 -ATPase activity by preferentially binding to an open catalytic site, consequently maintaining inhibitory MgADP in the adjacent closed catalytic site (22). Taken together, H_{NT} 's preference for EG1, as well as H_{CT} 's role in MgADP inhibition, indicated a potential interplay between the nucleotide occupancy of the catalytic sites and the interaction of $V_1\Delta H$ with H. To probe the effect of nucleotides on the interaction of H with $V_1\Delta H$, we again used BLI. $V_1\Delta H$ was bound to immobilized MBP-H, and the sensor was then dipped in wells containing buffer or buffer with 1 mM MgATP, MgADP + P_i , or MgAMPPNP. Interestingly, in the presence of MgATP, a biphasic dissociation curve was observed with an initial dissociation rate that was ~6 times faster than the rate in buffer alone (Fig. 6, A and B). However, only ~25% of the bound $V_1\Delta H$ dissociated with a fast rate with the remaining 75% coming off the sensor at a rate similar to the dissociation rate in buffer (Fig. 6, A and B). In contrast, a relatively slower rate of

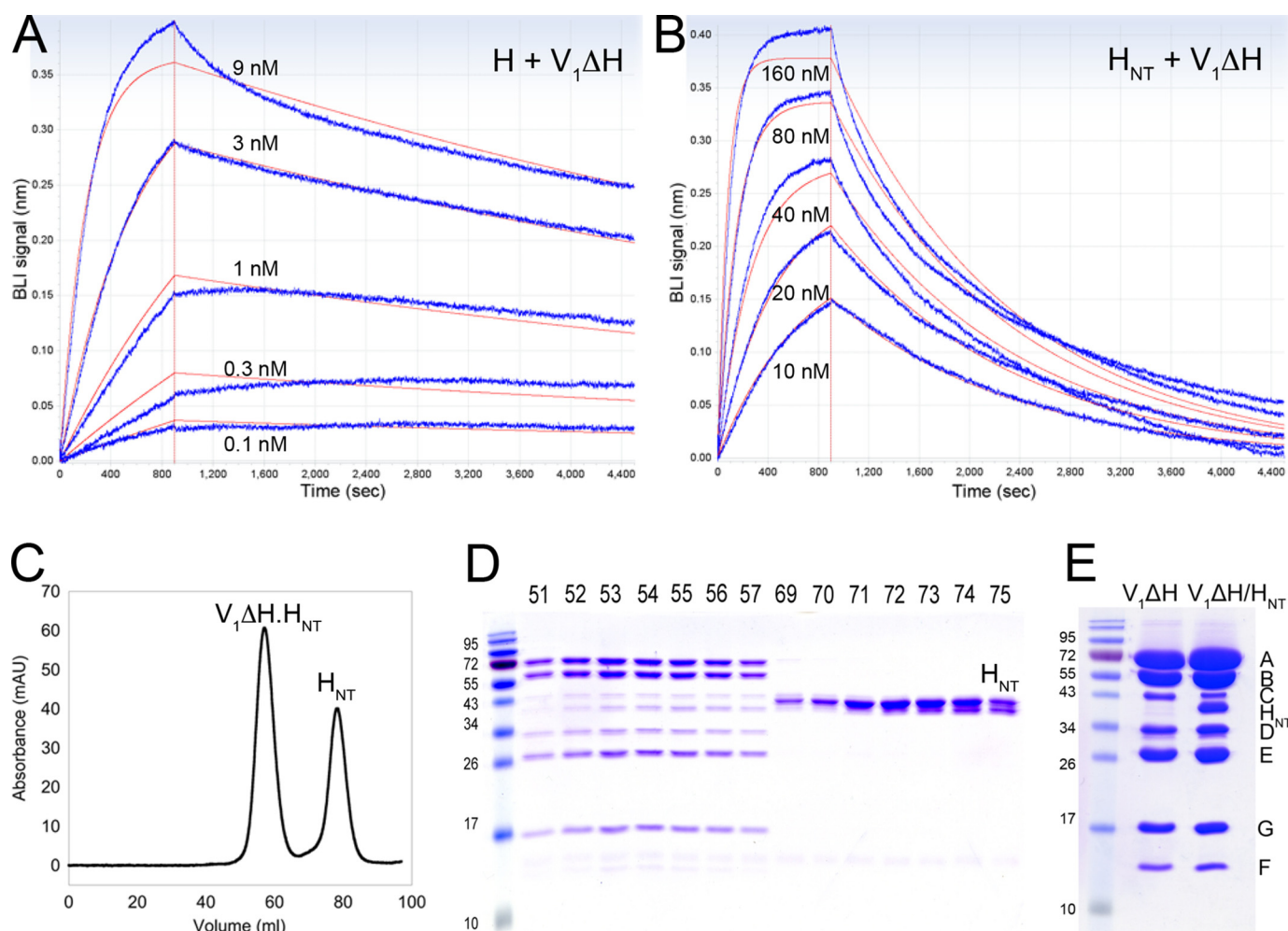


Figure 5. Interaction of H and H_{NT} with $V_1\Delta H$. *A*, the affinity of the interaction between H and $V_1\Delta H$ was determined using BLI at 22 °C in BLI buffer. Association and dissociation sensorgrams from five different concentrations of $V_1\Delta H$ (0.1, 0.3, 1, 3, and 9 nM) are shown in blue. The data were globally fit (traces in red) to reveal a K_d of ~ 65 μ M. *B*, a similar experiment was conducted to analyze the interaction between H_{NT} and $V_1\Delta H$. H_{NT} was dipped in 10, 20, 40, 80, and 160 nM $V_1\Delta H$ followed by buffer to generate association and dissociation curves, respectively (blue). The data were globally fit (red traces) to reveal a K_d of ~ 4.5 nM. *C*, $V_1\Delta H$ was incubated with a 5-fold excess of H_{NT} , and the mixture was resolved on a 1.6 \times 50-cm Superdex 200 column. *D*, SDS-PAGE of gel filtration fractions. The higher molecular weight peak showed $V_1\Delta H$ in complex with H_{NT} with the lower molecular weight peak corresponding to excess H_{NT} . *E*, approximately equimolar amounts of $V_1\Delta H$ and $V_1\Delta H$ in complex with H_{NT} were resolved by SDS-PAGE. The staining intensity of the H_{NT} compared with the single-copy subunit D band in the $V_1(\Delta H)H_{NT}$ complex suggests that $V_1\Delta H$ binds no more than one copy of H_{NT} with high affinity. *MAU*, milliabsorbance units.

dissociation was observed in the presence of MgADP + P_i and MgAMPPNP.

The destabilization of the V_1 -H interaction upon MgATP hydrolysis came as a surprise to us as the H subunit is known to inhibit V_1 -ATPase activity (22, 25, 39). To confirm that the fast dissociation of $V_1\Delta H$ from MBP-H in wells containing MgATP was specifically due to MgATP binding to V_1 's catalytic sites, we conducted a similar BLI experiment using $V_1\Delta H$ treated with *N*-ethylmaleimide (NEM). It is known that NEM modification of a catalytic-site cysteine residue prevents binding of nucleotides (42). NEM-treated and untreated $V_1\Delta H$ were bound to MBP-H immobilized on sensors and then dipped in wells containing MgATP, MgADP + P_i , or buffer (Fig. 6, C and D). We found that NEM-treated $V_1\Delta H$ no longer showed a fast dissociation rate when dipped in MgATP-containing wells, suggesting that MgATP binding to the catalytic sites caused destabilization of the V_1 -H interaction. However, if the above mentioned fast dissociation rate was a result of only MgATP binding, but not hydrolysis, we should have observed fast dis-

sociation in the presence of MgAMPPNP, the nonhydrolyzable ATP analog. MgAMPPNP, however, had no effect on the $V_1\Delta H$ dissociation rate (Fig. 6A, green trace). Taken together, the BLI experiments with NEM-modified $V_1\Delta H$ and in the presence of MgAMPPNP suggest that it is MgATP binding and hydrolysis that destabilize the V_1 -H interaction. Because both H_{NT} and H_{CT} contribute to the interaction of H with $V_1\Delta H$, we also measured the off-rate of $V_1\Delta H$ from immobilized MBP- H_{NT} and found that the H_{NT} - $V_1\Delta H$ interaction was also destabilized upon MgATP hydrolysis as seen for H and $V_1\Delta H$ (Fig. 6, E and F).

To verify that $V_1\Delta H$ bound to H was capable of transient turnover, we purified $V_1\Delta H$, incubated it with an excess of H, and resolved the mixture using size exclusion chromatography (Fig. S2). We found that $V_1\Delta H$ reconstituted with H ($V_1(\Delta H)H$) showed $\sim 4.9 \pm 0.55$ units/mg of MgATPase activity, which was $\sim 30\%$ of the activity of $V_1\Delta H$ (15.75 ± 1.7 units/mg) (Fig. 6G and Ref. 22). Considering the high-affinity interaction between $V_1\Delta H$ and H with a K_d of ~ 65 μ M, we expected stoichiometric

Subunit H interactions at the V_1-V_o interface

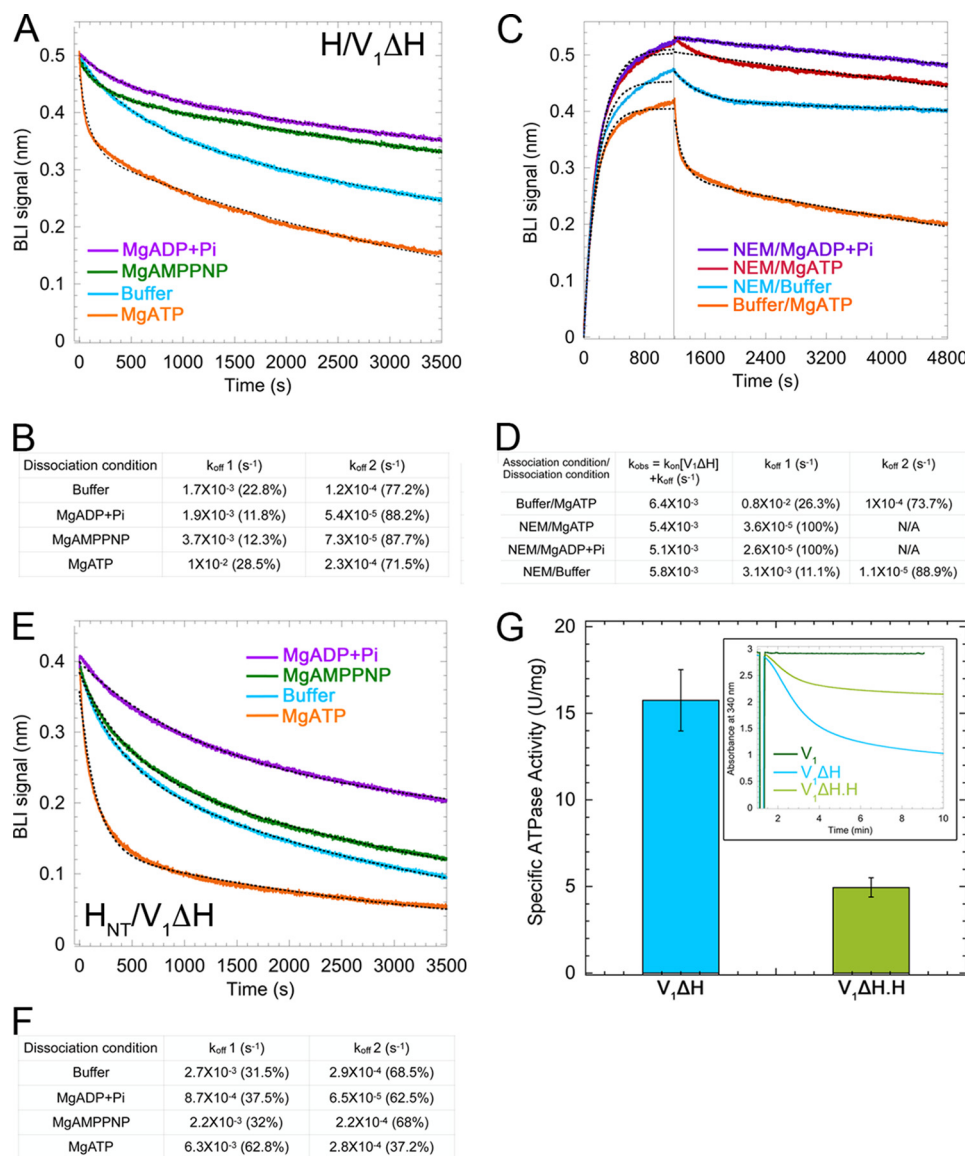


Figure 6. The interaction between subunit H and $V_1\Delta H$ is destabilized upon MgATP hydrolysis. *A*, sensorgrams of $V_1\Delta H$ dissociation from immobilized H subunit in the absence (*blue*) and presence of 1 mM nucleotides (MgADP + P_i , *purple*; MgAMPPNP, *green*; MgATP, *orange*). A representative from at least two independent experiments is shown. *B*, off-rates determined from fitting the sensorgrams from *A* to dual-exponential equations. *C*, sensorgrams of association and dissociation of NEM-inhibited $V_1\Delta H$ to and from immobilized H subunit in the absence or presence of 1 mM nucleotides (association of NEM-modified $V_1\Delta H$ in buffer/dissociation in MgADP + P_i , *purple*; association of NEM-modified $V_1\Delta H$ in buffer/dissociation in MgATP, *red*; both association and dissociation of NEM-modified $V_1\Delta H$ in buffer, *blue*; association of unmodified $V_1\Delta H$ in buffer/dissociation in MgATP, *orange*). A representative from at least two independent experiments is shown. *D*, observed on-rates (k_{obs}) and off-rates obtained from fitting the sensorgrams in *C* to single- and dual-exponential equations, respectively. *E*, sensorgrams of $V_1\Delta H$ dissociation from immobilized H_{NT} in the absence (*blue*) and presence of 1 mM nucleotides (MgADP + P_i , *purple*; MgAMPPNP, *green*; MgATP, *orange*). A representative from at least two independent experiments is shown. *F*, off-rates determined from fitting the sensorgrams from *E* to dual-exponential equations. *G*, average specific activities of $V_1\Delta H$ and $V_1(\Delta H)H$ plotted \pm S.E. (*error bars*) from two independent purifications. *Inset*, raw data for activity measurement using an ATP-regenerating assay (22). V_1 -ATPase activity is determined by monitoring a decrease in A_{340} as a function of time. Traces for WT V_1 , $V_1\Delta H$, and $V_1(\Delta H)H$ are shown in *dark green*, *blue*, and *light green*, respectively. *N/A*, not applicable.

amounts of H in the $V_1(\Delta H)H$ reconstituted complex. However, to exclude the possibility that the observed MgATPase activity in the $V_1(\Delta H)H$ complex was due to substoichiometric binding of H, we performed a pull-down experiment in which a 10-fold molar excess of MBP-H bound to amylose resin was used to capture $V_1\Delta H$ (Fig. S3). Although some MBP-H and $V_1\Delta H$ appeared in the supernatant and washes of the amylose resin, most of the MBP-H eluted in 10 mM maltose along with stoichiometrically bound $V_1\Delta H$. Elution fraction E1 (Fig. S3A) exhibited significant MgATPase activity (Fig. S3B), indicating

that a stoichiometric complex of $V_1\Delta H$ with MBP-H was capable of hydrolyzing MgATP.

A consistent feature of the dissociation curve of $V_1\Delta H$ from H in MgATP was its biphasic nature (Fig. 6A, *orange* trace), indicating that MgATP hydrolysis-dependent destabilization was transient. We found that, by using different concentrations of MgATP during dissociation, we were able to regulate the fast phase of the dissociation rate and consequently the duration of destabilization (Fig. 7). Not only does this experiment confirm MgATP hydrolysis as being the cause of V_1 -H destabilization,

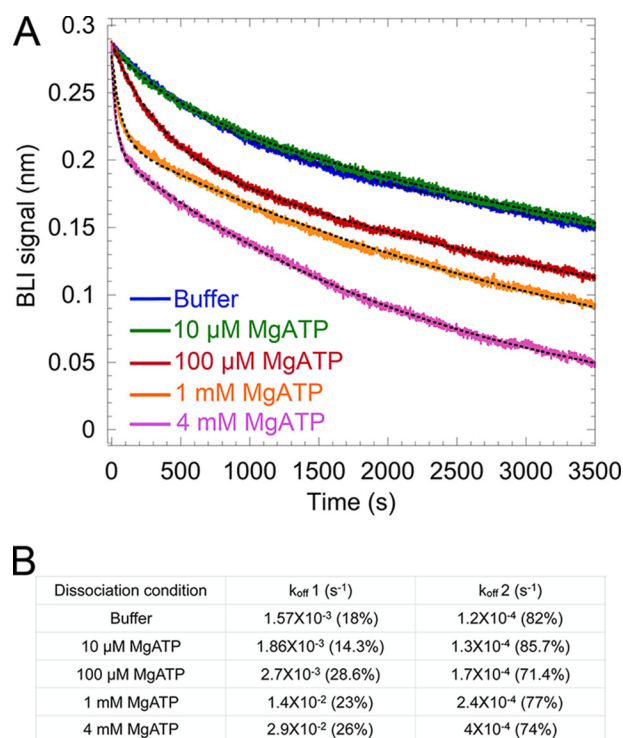


Figure 7. Modulation of the dissociation rate of $V_1\Delta H$ from H by varying the concentration of MgATP. A, sensorgrams of $V_1\Delta H$ dissociation from immobilized H subunit in the absence (blue) and presence of MgATP (10 μ M, purple; 100 μ M, red; 1 mM, orange; 4 mM, pink). A representative from two independent experiments is shown. B, off-rates determined by fitting the sensorgrams in A to dual-exponential equations.

it also explains why the destabilization is transient. Using P_i release-based ATPase assays, it has been shown that MgATPase activity of $V_1\Delta H$ subsides rapidly with time (25). This rapid decrease in activity, which is also observed in an ATP-regenerating assay (Fig. S4), has been attributed to the trapping of MgADP in a catalytic site, a phenomenon termed MgADP inhibition. We have observed that MgADP inhibition of $V_1\Delta H$ is more efficient under high Mg^{2+} (and by extension high MgATP) concentrations and that decreasing the initial concentration of MgATP results in delayed MgADP inhibition (Fig. S4). In the BLI experiment shown in Fig. 7, decreasing the concentration of MgATP to 100 μ M (Fig. 7, red trace) and consequently decreasing the rate of MgATP hydrolysis led to a delay in the culmination of the fast dissociation phase. Taken together, these data suggest that MgATP hydrolysis causes transient destabilization of the V_1 -H interaction until MgADP inhibition sets in.

Discussion

V-ATPase is regulated by reversible disassembly, a process that involves the breakage and reformation of several protein-protein interactions at the interface of V_1 and V_o . These interactions are mediated by the central rotor of V_1 (DF) binding to V_o 's subunit *d* and the three peripheral stalks (EG1-3) that link the collar subunits H and C to a_{NT} (see Fig. 2A). Both H and C are two domain proteins, and we previously found that C_{head} binds EG with high affinity, whereas C_{foot} and EG bind a_{NT} weakly. Here, we analyzed binding of H and H_{NT} to isolated EG, a_{NT} , and $V_1\Delta H$ purified from yeast. We found that the majority

of the binding energy between H and V_1 is contributed by the interaction between H_{NT} and EG and that binding of H_{NT} to EG is much stronger when EG is part of V_1 compared with isolated EG. However, only one copy of H_{NT} binds $V_1\Delta H$ with high affinity, indicating that the three EGs on V_1 are in different conformations and that only one of these conformations (EG1) is competent for H binding. The three different conformations of the EGs are evident from the crystal structure of autoinhibited V_1 (22) as well as the cryo-EM structures of V_1V_o (20, 21). The observation that H_{NT} binds only EG1 as part of V_1 with high affinity suggests that H_{NT} 's preference is a result, and not the cause, of the conformational asymmetry of the peripheral stalks, which most likely originates in the catalytic core of V_1 (A_3B_3DF). Although we were not able to detect an interaction between isolated H_{CT} and $V_1\Delta H$, the observation that intact H binds $V_1\Delta H$ with significantly higher affinity compared with H_{NT} suggests that the contact between H_{CT} and A_3B_3DF seen in the V_1 crystal structure (22) contributes to the avidity of the V_1 -H interaction. In addition, much like the C_{foot} - a_{NT} -EG low-affinity (but high-avidity) ternary junction, we found that H and a_{NT} interact weakly. Taken together, the data support and extend our earlier findings that V_1 and V_o are held together by multiple weak interactions that allow rapid breaking and reforming in response to cellular needs.

MgATP hydrolysis-dependent destabilization of the V_1 -H interaction

Studies in yeast have shown that membrane-detached V_1 has no measurable MgATPase activity, a property of WT V_1 that has been attributed to the presence of the inhibitory H subunit (25). Therefore, our BLI data showing that the V_1 -H interaction is destabilized in the presence of MgATP came as a surprise as we did not expect $V_1(\Delta H)H$ to be catalytically active. In contrast, previous biochemical studies had shown that $V_1\Delta H$ retained $\sim 20\%$ MgATPase activity upon addition of an excess of recombinant H, an observation that, at the time, was attributed to substoichiometric binding of H (39). However, using pulldown assays, we here show that a stoichiometric complex of $V_1\Delta H$ with H has indeed transient MgATPase activity, indicating that WT V_1 isolated from yeast is not equivalent to reconstituted $V_1(\Delta H)H$. One striking difference between V_1 and $V_1(\Delta H)H$ is that V_1 contains ~ 1.3 mol/mol of tightly bound ADP, whereas $V_1\Delta H$, and by extension $V_1(\Delta H)H$, has only ~ 0.4 mol/mol of ADP (22). This suggests that V_1 's ATPase activity is inhibited by tightly bound ADP and that the lack of ADP in $V_1(\Delta H)H$ allows transient MgATP hydrolysis with the associated conformational changes leading to destabilization of the V_1 -H interaction on the BLI sensor.

MgADP inhibition is a conserved feature of the catalytic headpiece of rotary ATPases wherein, under ATP-regenerating conditions, the rate of MgATP hydrolysis decreases due to retention of tightly bound MgADP at a closed catalytic site. The MgADP-inhibited state is a conformational off-pathway from the catalytic cycle and associated with a structural change in the catalytic site (43). MgADP inhibition has been observed in both the F_1 -ATPase (e.g. F_1 from bovine heart (44)) and *Bacillus* PS3 (45) and the cytosolic A_1/V_1 sector from *Thermus thermophilus* (46). Parra *et al.* (25) reported a decrease in MgATPase

Subunit H interactions at the V_1 - V_o interface

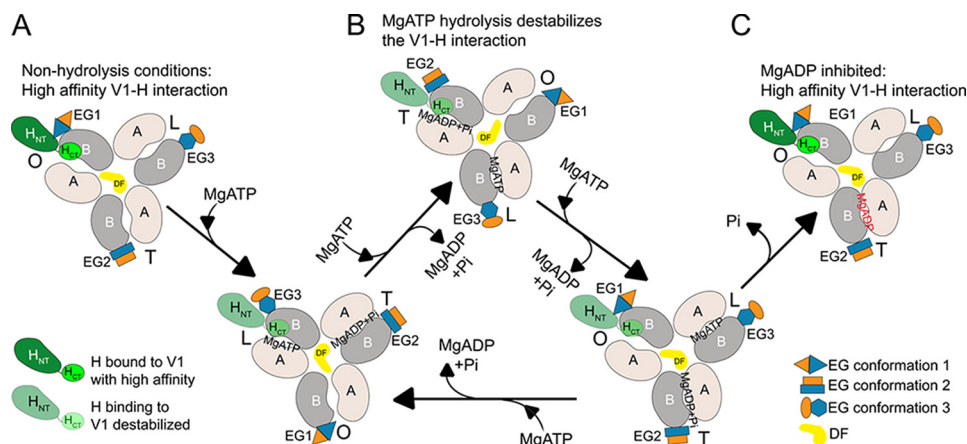


Figure 8. Model for the effect of MgATP hydrolysis on the V_1 -subunit H interaction. Shown is a view of V_1 from the membrane with H shown in green, peripheral stalk subunits EG in blue and orange, central rotor subunits DF in yellow, catalytic A subunit in tan, and B subunit in gray. $V_1\Delta H$ binds subunit H with high affinity in the absence of nucleotide (A). However, when MgATP is added to the system, it binds to the empty catalytic sites of V_1 , leading to MgATP hydrolysis (B). Cooperative and cyclical MgATP hydrolysis in V_1 leads to conformational changes in the three A/B pairs between open (O), loose (L), and tight (T) states. These cyclical switches of the A/B pairs are accompanied by structural changes in the associated EG heterodimers, which interchange between conformations denoted as EG1, EG2, and EG3. Because EG1 is the preferred binding site for H_{NT} , a change in conformation of EG1 to EG3 causes a destabilization of the EG- H_{NT} interaction. MgATP hydrolysis causes the counterclockwise rotation of the central rotor (DF) by $\sim 120^\circ$. Rotation of the central rotor along with conformational changes in the catalytic subunits causes destabilization of the V_1 - H_{CT} interaction. As observed in the BLI experiments, only a subset of the V_1 -H interactions are destabilized upon MgATP hydrolysis. The catalytic cycle stops once MgADP is bound in a tight site, causing MgADP inhibition. The V_1 -H interactions that withstand MgATP hydrolysis subsequently remain bound with high affinity under ADP-inhibited conditions (C).

activity of purified yeast $V_1\Delta H$ using P_i release assays, and we have observed a similar decrease in MgATPase activity of $V_1\Delta H$ using an ATP-regenerating assay system (22) (Fig. S4).

Interplay of MgADP inhibition with the V_1 -H interaction

The structure of autoinhibited V_1 revealed an inhibitory loop in H_{CT} (amino acids 408–414) that mediates important contacts with V_1 . First, H_{CT} binds to the C-terminal domain of subunit B, thereby stabilizing the corresponding catalytic A–B interface in its open conformation. Second, it interacts with two α -helical turns in the central rotor subunit D (residues 38–45) (22) (Fig. 2B). At any given rotational state of V_1 , only one of the catalytic sites is in the open state with the two α -helical turns from the central rotor facing the open site (22, 47). It is therefore evident that H_{CT} preferentially binds to the open catalytic site with the central rotor in a particular conformation. Our data suggest that the peripheral stalks exhibit a conformational asymmetry, which most likely originates from the conformations of the catalytic core of the enzyme (A_3B_3DF). H_{NT} preferentially interacts with EG1, the peripheral stalk associated with the open catalytic site. Under the conditions of our BLI experiments, when $V_1\Delta H$ is bound to subunit H on the sensor, both H_{NT} and H_{CT} are associated with their binding partners at the open catalytic site, resulting in overall tight binding of H as evident from the observed slow dissociation of $V_1\Delta H$ from the BLI sensor (Fig. 8A). When sensors containing $V_1\Delta H$ bound to MBP-H are dipped into MgATP, the nucleotide binds to the open catalytic site and is hydrolyzed. Subsequent MgATP hydrolysis results in central stalk rotation, which destabilizes the interaction with H_{CT} . The conformational changes are also propagated to the peripheral stalks, resulting in destabilization, and ultimately breaking, of the interaction between H_{NT} and EG1 (Fig. 8B). However, MgATP hydrolysis on $V_1(\Delta H)H$ is transient and stops once inhibitory MgADP gets trapped in a tight catalytic site. All the $V_1(\Delta H)H$ complexes that withstood

transient MgATP hydrolysis are now bound with high affinity because the binding site for H_{CT} is restored once the MgADP-inhibited conformation is obtained (Fig. 8C). Therefore, we conclude that the lack of inhibitory MgADP in $V_1(\Delta H)H$ allows transient MgATP hydrolysis and destabilization of the V_1 -H interaction and that high-affinity binding of H is restored once inhibitory MgADP is trapped in a catalytic site.

Considering the here observed MgATP hydrolysis-dependent destabilization of the interaction between H (and H_{NT}) with V_1 raises the question: how is this interaction maintained in V_1V_o during rotational catalysis? Between the three rotational states of the enzyme observed by cryo-EM (21), minor conformational differences are observed for the peripheral stalk bound to H (EG1 in V_1V_o). In V_1V_o , besides providing binding sites for both H_{NT} and H_{CT} , a_{NT} also interacts with and probably stabilizes the N termini of EG1 (Figs. 1A and 2A). The N-terminal region of the peripheral stalks have been described as unstable and flexible based on experiments conducted with isolated EG (33) and EG as part of A_1/V_1 (48) and as seen in the V_1 crystal structure (22). With EG1's N termini unsupported, as in membrane-detached V_1 , expected conformational changes associated with rotary catalysis would be larger than those observed in V_1V_o . Hence, although multiple interactions with a_{NT} maintain the conformation of EG1 in V_1V_o , the lack of these interactions in V_1 enable rotary catalysis-driven conformational changes in EG1 with concomitant destabilization of the H_{NT} -EG1 interaction.

Implications for the mechanism of reversible disassembly

Experiments conducted with yeast spheroplasts, isolated vacuoles, and purified V_1V_o have established that efficient disassembly of V-ATPase requires a catalytically active complex (49–51). From a structural comparison with the three rotational states of V_1V_o , we previously noted that upon disassembly of the holoenzyme autoinhibited V_1 and V_o end up in dif-

ferent rotational states: V_1 in state 2 and V_o in state 3 (22, 52, 53). This suggests that the MgATPase activity that is necessary for efficient disassembly serves to generate the rotational state mismatch associated with enzyme dissociation, a mismatch that likely functions to prevent rebinding of V_1 to V_o under cellular conditions that favor the disassembled state. It is well established that enzyme dissociation is accompanied by a release of subunit C into the cytosol, and it is possible that the energy from ATP hydrolysis also serves to break the high-affinity EG_{head} interaction (33). Live cell imaging has captured V_1 on vacuolar membranes while C is released into the cytosol upon glucose removal, suggesting that C release may be one of the initial steps of disassembly. Our data suggest that, due to catalysis-driven conformational changes in EG, membrane-detached V_1 sector is incapable of binding H in a stable conformation while MgATP is being hydrolyzed at the catalytic sites. Therefore, it is possible that V_1 detaches from V_o on vacuolar membranes after its MgATPase activity is completely silenced. The specificity of H_{NT} and H_{CT} for their binding sites on V_1 supports a model wherein once V_1 is MgADP-inhibited in rotational state 2 the proximity of the open catalytic site and central rotor favor H_{CT} 's conformational switch to its inhibitory position on V_1 . At the same time, by binding and stabilizing the open catalytic site, H_{CT} facilitates the trapping of MgADP in the adjacent closed catalytic site (22). Hence, inhibitory MgADP and subunit H synergize by stabilizing each other to ensure that free V_1 remains in the autoinhibited state to prevent wasteful ATP hydrolysis when V-ATPase's proton-pumping activity is down-regulated.

The autoinhibited state of V_1 (with MgADP in a closed catalytic site stabilized by H_{CT} bound to an open catalytic site) is likely a low-energy state of V_1 . For reassembly to occur, V_1 needs to be "reactivated" to allow H_{CT} to switch from its binding site on V_1 to bind a_{NT} in V_1V_o . Based on our observations in this study, we speculate that release of inhibitory MgADP and subsequent MgATP binding/hydrolysis induce structural changes in V_1 that detach H_{CT} , making it available to bind a_{NT} , in turn coupling V_1 to V_o . What then causes the required release of inhibitory MgADP from cytosolic V_1 ? Although this mechanism is currently not understood, it is possible that one of the protein factors that have been shown to be required for efficient reassembly, such as the regulator of the ATPase of vacuolar and endosomal membranes (RAVE) complex (54) or aldolase (55), plays a role in the release of inhibitory ADP, thereby allowing H_{CT} to assume its binding site on a_{NT} and restore MgATP hydrolysis-driven proton pumping.

Experimental procedures

Materials and methods

Plasmids encoding subunit H and its C-terminal domain (H_{CT} ; residues 352–478) N-terminally tagged with a Prescission protease-cleavable maltose-binding protein (MBP-H and MBP- H_{CT} encoded by a pMalPPase vector derived from pMAL-c2E), a yeast strain deleted for subunits H and G (39), and a pRS315 vector containing FLAG-tagged subunit G (56) were kind gifts from Dr. Patricia Kane, SUNY Upstate Medical University.

Plasmid construction

The plasmid expressing the N-terminal domain of subunit H (H_{NT} ; residues 1–354) was made using the above MBP-H pMalPPase vector as a template for QuikChange mutagenesis to delete the nucleotide sequence coding for amino acids 355–478 using the following primers: $H_{\text{NT}1-354}$ F, GGA AAT CCT AGA AAA CGA GTA CCA AGA ATT GAC CTA AAA GCT TGG CAC TGG CCG TCG TTT TAC AAC GTC G; $H_{\text{NT}1-354}$ R, GAC GGC CAG TGC CAA GCT TTT AGG TCA ATT CTT GGT ACT CGT TTT CTA GGA TTT CCT TG. The construction of the pMalPPase plasmid encoding N-terminally MBP-tagged a_{NT} (1–372) has been described (26).

Expression and purification of recombinant V-ATPase subunits

V-ATPase subunit constructs H_{NT} , EG, H_{CT} , H, and a_{NT} were expressed in *E. coli* strain Rosetta2, grown to midlog phase in rich broth (LB Miller plus 0.2% glucose) supplemented with ampicillin (100 $\mu\text{g}/\text{ml}$) and chloramphenicol (34 $\mu\text{g}/\text{ml}$). Protein expression was induced with 0.5 mM isopropyl β -D-thiogalactopyranoside (except for expression of EG where 1 mM isopropyl β -D-thiogalactopyranoside was used). Expression was induced at 30 °C for 6 h for H_{NT} , 20 °C for 6 h for H, 20 °C for \sim 16 h for a_{NT} , 25 °C for \sim 16 h for H_{CT} , and 30 °C for 6 h for EG. Cells were harvested by centrifugation, resuspended in amylose column buffer (CB; 20 mM Tris-HCl, 200 mM NaCl, 1 mM EDTA, pH 7.4), and stored at -20 °C until use. For purification, cells were treated with DNase (67 $\mu\text{g}/\text{ml}$), lysozyme (840 $\mu\text{g}/\text{ml}$), and PMSF (1 mM) before lysis by sonication. The lysate was then cleared by centrifugation at $12,000 \times g$ for 30 min, the supernatant was diluted 1:4 with CB and applied to an amylose affinity column at a rate of 1 ml/min, and nonspecifically bound material was removed by washing with 12 column volumes of CB followed by 15 column volumes of CB without NaCl. Bound protein was eluted using 25 ml of 10 mM maltose in CB without salt. The MBP tag was cleaved using Prescission protease as described (34). H, H_{CT} , and a_{NT} were separated from MBP by anion exchange chromatography (Mono Q) using a linear gradient of 0–300 mM NaCl in 25 mM Tris-HCl, 1 mM EDTA, pH 7, for elution. Residual MBP was removed by a small amylose column, and the concentrated protein was subjected to size exclusion chromatography using a Superdex S75 column (1.6×50 cm) for H and H_{CT} and a Superdex 200 column of the same size for a_{NT} . H_{NT} was separated from MBP using a gravity DEAE (anion exchange) column. At a pH of 6.5, MBP was immobilized on the DEAE column, and the H_{NT} flowed through. The flow-through was collected, concentrated, and subjected to size exclusion chromatography using a Superdex S75 column (1.6×50 cm). EG heterodimer was purified as described (33).

Purification of $V_1\Delta H$

V_1 -ATPase lacking subunit H was purified as described (22). Briefly, the yeast strain deleted for the genes encoding subunits H and G was transformed with a pRS315 plasmid encoding subunit G with an N-terminal FLAG tag (56). The cells were grown in synthetic defined medium lacking Leu to an OD of \sim 4.0 and harvested by centrifugation, and the cell pellets were resuspended in TBSE (25 mM Tris-HCl, pH 7.2, 150 mM NaCl, 0.5 mM EDTA) and stored at -80 °C until use. Thawed cells

Subunit H interactions at the V_1 - V_o interface

were supplemented with 5 mM β -mercaptoethanol, 1 mM PMSF, and 2 μ g/ml each of pepstatin and leupeptin before lysis by 15 passes through a microfluidizer with intermittent cooling on ice. The lysate was centrifuged at $4000 \times g$ for 25 min, and the resultant supernatant was centrifuged again at $13,000 \times g$ for 40 min. The cleared lysate was applied to a 5-ml FLAG column (Sigma) topped with Sephadex G50 and pre-equilibrated in TBSE. The column was washed with 10 column volumes of TBSE and eluted using 0.1 mg/ml FLAG peptide. $V_1\Delta H$ -containing fractions were pooled, concentrated, and resolved using a Superdex 200 1.6×50 -cm column attached to an ÄKTA FPLC (GE Healthcare). Fractions were analyzed by SDS-PAGE and concentrated to 10 mg/ml, and the activity of the complex was measured using a coupled enzyme assay as described below (22).

CD spectroscopy

CD spectra were recorded on an Aviv 202 spectropolarimeter using a 2-mm-path length cuvette. CD spectra were recorded between 250 and 195 nm in 25 mM sodium phosphate, pH 7, and protein stability was monitored by recording the CD signal at 222 nm as a function of temperature. For cysteine-containing proteins, 0.3–1 mM TCEP was included in the buffer. Protein concentrations of H, H_{NT} , H_{CT} , and a_{NT} were 2, 2.25, 9.2, and 2.36 μ M, respectively. The far-UV CD spectrum of 6.7 μ M H_{NT} -EG complex was obtained with protein dissolved in 20 mM Tris-HCl, 1 mM TCEP, pH 8 buffer at 4 °C followed by monitoring the temperature dependence of the CD signal at 222 nm.

Isothermal titration calorimetry

The thermodynamic parameters of the interaction between H_{NT} and EG and between H_{CT} and a_{NT} were determined using a Microcal VP-ITC isothermal titration calorimeter. The interaction of H_{NT} and EG was monitored by titrating a stock of 0.278 mM H_{NT} into 0.0315 mM EG in 20 mM Tris-HCl, 0.5 mM EDTA, 1 mM TCEP, pH 8, at 10 °C. A total of 30 injections with 5% saturation per injection was carried out. The average value of signal postsaturation (last eight titration points) was subtracted from the H_{NT} into EG titration. Complex formation between a_{NT} and H was analyzed by titrating 0.3 mM H into 0.017 mM a_{NT} in 20 mM Tris-HCl, 0.5 mM EDTA, 1 mM TCEP, pH 8. A blank titration of H into buffer was subtracted from the a_{NT} into H titration using the curve fit option in OriginLab. ITC data were analyzed using VP-ITC programs in OriginLab.

Biolayer interferometry

BLI was used to measure the association and dissociation kinetics of interaction between $V_1\Delta H$ and MBP-tagged H, H_{NT} , and H_{CT} . An Octed-RED system and AMC-coated sensors (FortéBio, AMC biosensors, catalogue number 18-5088) were used to monitor protein-protein binding and dissociation for determination of binding affinities. Anti-MBP antibody (New England Biolabs) at 1 μ g/ml was immobilized on the AMC biosensors. The anti-MBP antibody formed the bait for MBP-tagged H, H_{NT} , and H_{CT} (used at 5 μ g/ml). Biosensors with immobilized H, H_{NT} , or H_{CT} were dipped in varying concentrations of $V_1\Delta H$ followed by buffer to measure association and

dissociation rates. BLI buffer (20 mM Tris-HCl, pH 7.2, 150 mM NaCl, 1 mM EDTA, 0.5 mg/ml BSA) was used in all BLI experiments to reduce nonspecific binding to the biosensors except for experiments in the presence of nucleotides where the EDTA concentration was reduced to 0.5 mM. All steps were done at 22 °C with each biosensor agitated in 0.2 ml of sample at 1000 rpm and a standard measurement rate of 5 s^{-1} . Control experiments were performed to check for any nonspecific binding interaction between the antibodies and the proteins used. Reference sensors were used in each experiment with immobilized MBP-H/ H_{NT} / H_{CT} but no $V_1\Delta H$. FortéBio data analysis software (version 6.4) was used for subtraction of reference sensors, Savitzky-Golay filtering, and global fitting of the kinetic rates of $V_1\Delta H$ binding with H, H_{NT} , or H_{CT} .

ATPase activity assays

MgATPase activity of V_1 , $V_1\Delta H$, and $V_1(\Delta H)H$ was measured using an ATP-regenerating assay as described (22). Briefly, 10 μ g of the V_1 mutant was added to an assay mixture containing 1 mM MgCl_2 , 5 mM ATP, 30 units/ml each of lactate dehydrogenase and pyruvate kinase, 0.5 mM NADH, 2 mM phosphoenolpyruvate, 50 mM HEPES, pH 7.5, at 37 °C. The decrease of absorbance at 340 nm was measured in the kinetics mode on a Varian Cary Bio100 spectrophotometer.

Native gel electrophoresis

For native gel electrophoresis, purified V-ATPase subunits and subcomplexes were resolved using 2% agarose gels in 20 mM bis-Tris-acetic acid, pH 6, 1 mM TCEP. Gels were resolved for 1 h at 100 V, fixed in 25% isopropanol, 10% acetic acid for 30 minutes, rinsed in 95% ethanol, and dried on a slab dryer for 2 h at 80 °C. The dried gel was stained with Coomassie G and destained in fixing solution.

Author contributions—S. S., R. A. O., and S. W. conceptualization; S. S. data curation; S. S. formal analysis; S. S. validation; S. S. investigation; S. S. visualization; S. S. and R. A. O. methodology; S. S. writing-original draft; S. S., R. A. O., and S. W. writing-review and editing; R. A. O. and S. W. supervision; S. W. funding acquisition; S. W. project administration.

Acknowledgments—We thank Dr. Patricia Kane for reagents, Dr. Stewart Loh for assistance with CD data collection, and Dr. Thomas Duncan for assistance with BLI data collection and analysis.

References

1. Forgac, M. (2007) Vacuolar ATPases: rotary proton pumps in physiology and pathophysiology. *Nat. Rev. Mol. Cell Biol.* **8**, 917–929 [CrossRef Medline](#)
2. Frattini, A., Orchard, P. J., Sobacchi, C., Giliani, S., Abinun, M., Mattsson, J. P., Keeling, D. J., Andersson, A. K., Wallbrandt, P., Zecca, L., Notarangelo, L. D., Vezzoni, P., and Villa, A. (2000) Defects in TCIRG1 subunit of the vacuolar proton pump are responsible for a subset of human autosomal recessive osteopetrosis. *Nat. Genet.* **25**, 343–346 [CrossRef Medline](#)
3. Thudium, C. S., Jensen, V. K., Karsdal, M. A., and Henriksen, K. (2012) Disruption of the V-ATPase functionality as a way to uncouple bone formation and resorption—a novel target for treatment of osteoporosis. *Curr. Protein Pept. Sci.* **13**, 141–151 [CrossRef Medline](#)

4. Karet, F. E., Finberg, K. E., Nelson, R. D., Nayir, A., Mocan, H., Sanjad, S. A., Rodriguez-Soriano, J., Santos, F., Cremers, C. W., Di Pietro, A., Hoffbrand, B. I., Winiarski, J., Bakkaloglu, A., Ozen, S., Dusunsell, R., *et al.* (1999) Mutations in the gene encoding B1 subunit of H^+ -ATPase cause renal tubular acidosis with sensorineural deafness. *Nat. Genet.* **21**, 84–90 [CrossRef Medline](#)
5. Brown, D., Smith, P. J., and Breton, S. (1997) Role of V-ATPase-rich cells in acidification of the male reproductive tract. *J. Exp. Biol.* **200**, 257–262 [Medline](#)
6. Williamson, W. R., and Hiesinger, P. R. (2010) On the role of v-ATPase V_{0a1} -dependent degradation in Alzheimer disease. *Commun. Integr. Biol.* **3**, 604–607 [CrossRef Medline](#)
7. Sun-Wada, G. H., Toyomura, T., Murata, Y., Yamamoto, A., Futai, M., and Wada, Y. (2006) The $\alpha 3$ isoform of V-ATPase regulates insulin secretion from pancreatic β -cells. *J. Cell Sci.* **119**, 4531–4540 [CrossRef Medline](#)
8. Lu, X., Yu, H., Liu, S. H., Brodsky, F. M., and Peterlin, B. M. (1998) Interactions between HIV1 Nef and vacuolar ATPase facilitate the internalization of CD4. *Immunity* **8**, 647–656 [CrossRef Medline](#)
9. Sennoune, S. R., Bakunts, K., Martínez, G. M., Chua-Tuan, J. L., Kebir, Y., Attaya, M. N., and Martínez-Zaguilán, R. (2004) Vacuolar H^+ -ATPase in human breast cancer cells with distinct metastatic potential: distribution and functional activity. *Am. J. Physiol. Cell Physiol.* **286**, C1443–C1452 [CrossRef Medline](#)
10. Kane, P. M. (2012) Targeting reversible disassembly as a mechanism of controlling V-ATPase activity. *Curr. Protein Pept. Sci.* **13**, 117–123 [CrossRef Medline](#)
11. Fais, S., De Milito, A., You, H., and Qin, W. (2007) Targeting vacuolar H^+ -ATPases as a new strategy against cancer. *Cancer Res.* **67**, 10627–10630 [CrossRef Medline](#)
12. Wilkens, S. (2005) Rotary molecular motors. *Adv. Protein Chem.* **71**, 345–382 [CrossRef Medline](#)
13. Muench, S. P., Trinick, J., and Harrison, M. A. (2011) Structural divergence of the rotary ATPases. *Q. Rev. Biophys.* **44**, 311–356 [CrossRef Medline](#)
14. Futai, M., Nakanishi-Matsui, M., Okamoto, H., Sekiya, M., and Nakamoto, R. K. (2012) Rotational catalysis in proton pumping ATPases: from *E. coli* F-ATPase to mammalian V-ATPase. *Biochim. Biophys. Acta* **1817**, 1711–1721 [CrossRef Medline](#)
15. Kitagawa, N., Mazon, H., Heck, A. J., and Wilkens, S. (2008) Stoichiometry of the peripheral stalk subunits E and G of yeast V_1 -ATPase determined by mass spectrometry. *J. Biol. Chem.* **283**, 3329–3337 [CrossRef Medline](#)
16. Powell, B., Graham, L. A., and Stevens, T. H. (2000) Molecular characterization of the yeast vacuolar H^+ -ATPase proton pore. *J. Biol. Chem.* **275**, 23654–23660 [CrossRef Medline](#)
17. Mazhab-Jafari, M. T., Rohou, A., Schmidt, C., Bueler, S. A., Benlekbir, S., Robinson, C. V., and Rubinstein, J. L. (2016) Atomic model for the membrane-embedded V_o motor of a eukaryotic V-ATPase. *Nature* **539**, 118–122 [CrossRef Medline](#)
18. Wilkens, S., Inoue, T., and Forgac, M. (2004) Three-dimensional structure of the vacuolar ATPase. Localization of subunit H by difference imaging and chemical cross-linking. *J. Biol. Chem.* **279**, 41942–41949 [CrossRef Medline](#)
19. Zhang, Z., Zheng, Y., Mazon, H., Milgrom, E., Kitagawa, N., Kish-Trier, E., Heck, A. J., Kane, P. M., and Wilkens, S. (2008) Structure of the yeast vacuolar ATPase. *J. Biol. Chem.* **283**, 35983–35995 [CrossRef Medline](#)
20. Rawson, S., Phillips, C., Huss, M., Tiburcy, F., Wiczorek, H., Trinick, J., Harrison, M. A., and Muench, S. P. (2015) Structure of the vacuolar H^+ -ATPase rotary motor reveals new mechanistic insights. *Structure* **23**, 461–471 [CrossRef Medline](#)
21. Zhao, J., Benlekbir, S., and Rubinstein, J. L. (2015) Electron cryomicroscopy observation of rotational states in a eukaryotic V-ATPase. *Nature* **521**, 241–245 [CrossRef Medline](#)
22. Oot, R. A., Kane, P. M., Berry, E. A., and Wilkens, S. (2016) Crystal structure of yeast V_1 -ATPase in the autoinhibited state. *EMBO J.* **35**, 1694–1706 [CrossRef Medline](#)
23. Zhang, J., Feng, Y., and Forgac, M. (1994) Proton conduction and bafilomycin binding by the V_o domain of the coated vesicle V-ATPase. *J. Biol. Chem.* **269**, 23518–23523 [Medline](#)
24. Gräf, R., Harvey, W. R., and Wiczorek, H. (1996) Purification and properties of a cytosolic V_1 -ATPase. *J. Biol. Chem.* **271**, 20908–20913 [CrossRef Medline](#)
25. Parra, K. J., Keenan, K. L., and Kane, P. M. (2000) The H subunit (Vma13p) of the yeast V-ATPase inhibits the ATPase activity of cytosolic V_1 complexes. *J. Biol. Chem.* **275**, 21761–21767 [CrossRef Medline](#)
26. Couoh-Cardel, S., Milgrom, E., and Wilkens, S. (2015) Affinity purification and structural features of the yeast vacuolar ATPase V_o membrane sector. *J. Biol. Chem.* **290**, 27959–27971 [CrossRef Medline](#)
27. Kane, P. M. (1995) Disassembly and reassembly of the yeast vacuolar H^+ -ATPase *in vivo*. *J. Biol. Chem.* **270**, 17025–17032 [Medline](#)
28. Sumner, J. P., Dow, J. A., Earley, F. G., Klein, U., Jäger, D., and Wiczorek, H. (1995) Regulation of plasma membrane V-ATPase activity by dissociation of peripheral subunits. *J. Biol. Chem.* **270**, 5649–5653 [CrossRef Medline](#)
29. Trombetta, E. S., Ebersold, M., Garrett, W., Pypaert, M., and Mellman, I. (2003) Activation of lysosomal function during dendritic cell maturation. *Science* **299**, 1400–1403 [CrossRef Medline](#)
30. Sautin, Y. Y., Lu, M., Gaugler, A., Zhang, L., and Gluck, S. L. (2005) Phosphatidylinositol 3-kinase-mediated effects of glucose on vacuolar H^+ -ATPase assembly, translocation, and acidification of intracellular compartments in renal epithelial cells. *Mol. Cell. Biol.* **25**, 575–589 [CrossRef Medline](#)
31. Lafourcade, C., Sobo, K., Kieffer-Jaquinod, S., Garin, J., and van der Goot, F. G. (2008) Regulation of the V-ATPase along the endocytic pathway occurs through reversible subunit association and membrane localization. *PLoS One* **3**, e2758 [CrossRef Medline](#)
32. Stransky, L. A., and Forgac, M. (2015) Amino acid availability modulates vacuolar H^+ -ATPase assembly. *J. Biol. Chem.* **290**, 27360–27369 [CrossRef Medline](#)
33. Oot, R. A., and Wilkens, S. (2010) Domain characterization and interaction of the yeast vacuolar ATPase subunit C with the peripheral stator stalk subunits E and G. *J. Biol. Chem.* **285**, 24654–24664 [CrossRef Medline](#)
34. Oot, R. A., and Wilkens, S. (2012) Subunit interactions at the V_1 - V_o interface in yeast vacuolar ATPase. *J. Biol. Chem.* **287**, 13396–13406 [CrossRef Medline](#)
35. Curtis, K. K., Francis, S. A., Oluwatosin, Y., and Kane, P. M. (2002) Mutational analysis of the subunit C (Vma5p) of the yeast vacuolar H^+ -ATPase. *J. Biol. Chem.* **277**, 8979–8988 [CrossRef Medline](#)
36. Ho, M. N., Hirata, R., Umamoto, N., Ohya, Y., Takatsuki, A., Stevens, T. H., and Anraku, Y. (1993) VMA13 encodes a 54-kDa vacuolar H^+ -ATPase subunit required for activity but not assembly of the enzyme complex in *Saccharomyces cerevisiae*. *J. Biol. Chem.* **268**, 18286–18292 [Medline](#)
37. Liu, M., Tarsio, M., Charsky, C. M., and Kane, P. M. (2005) Structural and functional separation of the N- and C-terminal domains of the yeast V-ATPase subunit H. *J. Biol. Chem.* **280**, 36978–36985 [CrossRef Medline](#)
38. Sagermann, M., Stevens, T. H., and Matthews, B. W. (2001) Crystal structure of the regulatory subunit H of the V-type ATPase of *Saccharomyces cerevisiae*. *Proc. Natl. Acad. Sci. U.S.A.* **98**, 7134–7139 [CrossRef Medline](#)
39. Diab, H., Ohira, M., Liu, M., Cobb, E., and Kane, P. M. (2009) Subunit interactions and requirements for inhibition of the yeast V_1 -ATPase. *J. Biol. Chem.* **284**, 13316–13325 [CrossRef Medline](#)
40. Lu, M., Vergara, S., Zhang, L., Holliday, L. S., Aris, J., and Gluck, S. L. (2002) The amino-terminal domain of the E subunit of vacuolar H^+ -ATPase (V-ATPase) interacts with the H subunit and is required for V-ATPase function. *J. Biol. Chem.* **277**, 38409–38415 [CrossRef Medline](#)
41. Isaka, Y., Ekimoto, T., Kokabu, Y., Yamato, I., Murata, T., and Ikeguchi, M. (2017) Rotation mechanism of molecular motor V_1 -ATPase studied by multiscale molecular dynamics simulation. *Biophys. J.* **112**, 911–920 [CrossRef Medline](#)
42. Liu, Q., Leng, X. H., Newman, P. R., Vasilyeva, E., Kane, P. M., and Forgac, M. (1997) Site-directed mutagenesis of the yeast V-ATPase A subunit. *J. Biol. Chem.* **272**, 11750–11756 [CrossRef Medline](#)
43. Kishikawa, J., Nakanishi, A., Furuike, S., Tamakoshi, M., and Yokoyama, K. (2014) Molecular basis of ADP inhibition of vacuolar (V)-type ATPase/synthase. *J. Biol. Chem.* **289**, 403–412 [CrossRef Medline](#)

Subunit H interactions at the V_1 - V_0 interface

44. Vasilyeva, E. A., Minkov, I. B., Fitin, A. F., and Vinogradov, A. D. (1982) Kinetic mechanism of mitochondrial adenosine triphosphatase. Inhibition by azide and activation by sulphite. *Biochem. J.* **202**, 15–23 [CrossRef Medline](#)
45. Jault, J. M., Dou, C., Grodsky, N. B., Matsui, T., Yoshida, M., and Allison, W. S. (1996) The $\alpha 3\beta 3\gamma$ subcomplex of the F_1 -ATPase from the thermophilic *Bacillus* PS3 with the $\beta T165S$ substitution does not entrap inhibitory MgADP in a catalytic site during turnover. *J. Biol. Chem.* **271**, 28818–28824 [CrossRef Medline](#)
46. Nakano, M., Imamura, H., Toei, M., Tamakoshi, M., Yoshida, M., and Yokoyama, K. (2008) ATP hydrolysis and synthesis of a rotary motor V-ATPase from *Thermus thermophilus*. *J. Biol. Chem.* **283**, 20789–20796 [CrossRef Medline](#)
47. Arai, S., Saijo, S., Suzuki, K., Mizutani, K., Kakinuma, Y., Ishizuka-Katsura, Y., Ohsawa, N., Terada, T., Shirouzu, M., Yokoyama, S., Iwata, S., Yamato, I., and Murata, T. (2013) Rotation mechanism of *Enterococcus hirae* V1-ATPase based on asymmetric crystal structures. *Nature* **493**, 703–707 [CrossRef Medline](#)
48. Zhou, M., Politis, A., Davies, R., Liko, I., Wu, K. J., Stewart, A. G., Stock, D., and Robinson, C. V. (2014) Ion mobility-mass spectrometry of a rotary ATPase reveals ATP-induced reduction in conformational flexibility. *Nat. Chem.* **6**, 208–215 [CrossRef Medline](#)
49. Parra, K. J., and Kane, P. M. (1998) Reversible association between the V1 and V0 domains of yeast vacuolar H^+ -ATPase is an unconventional glucose-induced effect. *Mol. Cell. Biol.* **18**, 7064–7074 [CrossRef Medline](#)
50. MacLeod, K. J., Vasilyeva, E., Merdek, K., Vogel, P. D., and Forgacs, M. (1999) Photoaffinity labeling of wild-type and mutant forms of the yeast V-ATPase A subunit by 2-azido- $[^{32}P]$ ADP. *J. Biol. Chem.* **274**, 32869–32874 [CrossRef Medline](#)
51. Sharma, S., and Wilkens, S. (2017) Biolayer interferometry of lipid nanodisc-reconstituted yeast vacuolar H^+ -ATPase. *Protein Sci.* **26**, 1070–1079 [CrossRef Medline](#)
52. Stam, N. J., and Wilkens, S. (2017) Structure of the lipid nanodisc-reconstituted vacuolar ATPase proton channel: definition of the interaction of rotor and stator and implications for enzyme regulation by reversible dissociation. *J. Biol. Chem.* **292**, 1749–1761 [CrossRef Medline](#)
53. Oot, R. A., Couoh-Cardel, S., Sharma, S., Stam, N. J., and Wilkens, S. (2017) Breaking up and making up: the secret life of the vacuolar H^+ -ATPase. *Protein Sci.* **26**, 896–909 [CrossRef Medline](#)
54. Smardon, A. M., Tarsio, M., and Kane, P. M. (2002) The RAVE complex is essential for stable assembly of the yeast V-ATPase. *J. Biol. Chem.* **277**, 13831–13839 [CrossRef Medline](#)
55. Lu, M., Ammar, D., Ives, H., Albrecht, F., and Gluck, S. L. (2007) Physical interaction between aldolase and vacuolar H^+ -ATPase is essential for the assembly and activity of the proton pump. *J. Biol. Chem.* **282**, 24495–24503 [CrossRef Medline](#)
56. Zhang, Z., Charsky, C., Kane, P. M., and Wilkens, S. (2003) Yeast V1-ATPase: affinity purification and structural features by electron microscopy. *J. Biol. Chem.* **278**, 47299–47306 [CrossRef Medline](#)